PERGAMON

International Journal of Mechanical Sciences 44 (2002) 1145–1161

International Journal of MECHANICAL SCIENCES

www.elsevier.com/locate/ijmecsci

Modes of axial collapse of unconstrained capped frusta

A.A.A. Alghamdi*, A.A.N. Aljawi, T.M.-N. Abu-Mansour

Department of Mechanical Engineering, King Abdulaziz University, P.O. Box 80204, Jeddah 21589, Saudi Arabia

Received 8 October 2001

Abstract

Efforts are made to classify the modes of deformation of unconstrained capped end frusta when crushed axially between two parallel plates. Tens of aluminum spun capped end frusta of different semi-apex angles (15–60°) and thicknesses (1–3 mm) are crushed at quasi-static loading conditions using a universal instron machine. The resulting modes of deformation can be classified into: (1) outward inversion, (2) limited inward inversion followed by outward inversion, (3) full inward inversion followed by outward inversion, (4) limited extensible crumpling followed by outward inversion, and (5) full extensible crumpling. Samples of frusta made of low carbon steel sheets and nylon plastic were tested statically and gave similar results. An explicit version of ABAQUS 5.8 finite element (FE) program is used to model the crushing modes. Good agreement is obtained between the FE predictions and the experimental work. © 2002 Elsevier Science Ltd. All rights reserved.

Keywords: Frusta; Energy absorbers; ABAQUS

1. Introduction

Energy absorbers are systems that convert kinetic energy into other forms of energy, such as plastic deformation energy in deformable solids. The process of conversion in plastic deformation depends on the magnitude and the method of application of loads, transmission rates, deformation displacement patterns and material properties such as ductility and toughness.

The predominant domain of applications of collapsible energy absorbers is that of crash protection. Such systems are installed in high-risk environments with potential injury to humans or damage to property. The active absorbing element of an energy absorption system can assume several common shapes such as circular tubes [4], square tubes [5,6] and frusta [1–3].

Axisymmetrical and circular shapes provide perhaps the widest range of all choices for use as absorbing elements because of their favorable plastic behavior under axial forces, as well as their

* Corresponding author. Tel.: +996-5-564-1233; fax: +966-2-695-2193.

E-mail address: aljinaidi@hotmail.com (A.A.A. Alghamdi).

PII: S0020-7403(02)00018-8

Nomenclature

d	small diameter of the frustum, m
D	large diameter of the frustum, m
D_m	mean diameter of the frustum, m
e	specific energy, J/g
E	absorbed energy during crushing, Joule
H	Overall height of the frustum, m
P_{av}	average crushing force, N
t	wall thickness of the frusta, m
x	displacement, m
Y	Yield strength, N/m^2
Φ	semi-apical angle, deg

common occurrence as structural elements. Axial crushing of frusta as impact absorbers has been investigated for decades [1–3]. In this paper, the selected absorber has a truncated capped frustum shape that is employed over a wide range of applications.

2. Axial crushing of thin frusta

Frusta (truncated circular cones) have a wide range of applications. The occurrence of frusta as structural members has drawn some attention, especially due to their stable plastic behavior when crushed axially. The literature on this topic, however, is generally meagre [2].

One of the early studies of frustum (truncated circular cone) was carried out by Postlethwaite and Mills [1]. In their study of axial crushing of conical shells they used Alexander's extensible collapse analysis [4] for rigid-perfectly material cones. They reported the mean crushing force (P_{av}) for external collapse as

$$P_{av} = 6Yt^{3/2}\sqrt{d + 2x\sin(\phi)} + 5.69Yt^2\tan(\phi) \tag{1}$$

where Y is the yield strength, t is the frustum wall thickness, x is the deformation along the axis of the frustum, d is the small diameter of the frustum and ϕ is the semi-apical angle of the frustum.

Mamalis and Johnson [2] experimentally investigated the quasi-static crumpling of aluminum tubes and frusta under quasi-static compression. Their main objective was, among other things, to determine the experimental details of the failure modes of frusta with the small semi-apical angles of $\phi = 5^\circ$ and 10°. It was observed that load–deflection curves of the frusta are more regular than those of cylinders. Also, post-buckling load increases in a parabolic manner with increase in wall thickness, and, as expected, post-buckling load decreases with increase in semi-apical angle. It was observed that thin frusta deformed into an extensible collapse diamond shape whereas thick ones deformed into axisymmetric rings. The authors fitted empirical equations to their results for both concertina and diamond modes of deformation.

Mamalis et al. [7] repeated the same experimental study using low-carbon steel at the compression rate of 2.5 m/min. It was observed that the initial axisymmetric bellows changes into non-symmetric diamond shapes and the number of lobes of the diamond shape increases as the ratio of the mean diameter/thickness increases.

Mamalis et al. [8] proposed an extensible theoretical model to predict the plastically dissipated energy and the mean post-buckling load for axially crumpled thin walled circular cones and frusta for the concertina mode of deformation. The theoretical model was based on a consideration of the plastic work dissipated in plastic hinges and in stretching of material between them without considering their interaction. The model gave the average crushing load in the form,

$$P_{\mathrm{av}} = 6Yt^{3/2}(\sqrt{d} + 0.95\sqrt{t}\tan(\phi)) \tag{2}$$

The predicted average crushing loads were in fair agreement with the experimental results.

Mamalis et al. [9] developed a theoretical model to predict the mean crushing load for axially loaded circular cones and frusta deformed into the diamond mode of deformation. The model was based on the inextensional model developed by Johnson et al. [10].

Mamalis et al. [11] improved the analytical model for the concertina mode of deformation by making it capable of predicting the deformation history of thin-wall tubes and frusta. They obtained long and tedious equations for internally and externally formed convolutions, which were in fair agreement with the experimental curves.

Mamalis et al. [12] studied the axial crushing of thin PVC frusta of square cross-sections. A theoretical model for prediction of the average crushing force was developed on the basis of an inextensional folding mechanism of the diamond mode of deformation. Good correlation between the experimental and analytical results was shown.

Mamalis et al. investigated the axial collapse of composite tubes [13] and frusta of square [14] and circular [15] sections and developed an analytical model of the crushing stages based on actual experimental observation.

Alghamdi [16] introduced two innovative modes of deformations for frusta. The first one is direct inversion [17] and the other one is outward flattening. Using the ABAQUS finite element program, Aljawi and Alghamdi [18] modeled the collapse of frusta when inverted. Good agreement was obtained between experimental results and theoretical predictions. Aljawi and Alghamdi [19] further investigated the details of the inversion of frusta when crushed axially. Alghamdi et al. [20] presented the details of crushing of spun aluminum frusta between two parallel plates. They reported that their predictions using ABAQUS were in good agreement with experimental results.

Most of the above studies, except Alghamdi et al. [20], deal with axial crushing (or crumbling) of frusta with small semi-apical angle (15° maximum) between two parallel plates. However, the present paper investigates the quasi-static crushing of frusta with large range of semi-apical angles (15–60°) and different thicknesses and materials and classifies the deformation modes. Also, this paper summarizes the work that has been done in relation to axial crushing of frusta in Refs. [16,18,20] and the present is in a complete and final shape.

3. Finite element modeling

In the present study, ABAQUS Explicit FE code (version 5.8) [21] is employed to investigate the axial deformation modes of frusta under quasi-static loading. An axisymmetric four-noded element, CAX4R, is used for modeling the frustum shown in Fig. 1. About 300 elements are used for the

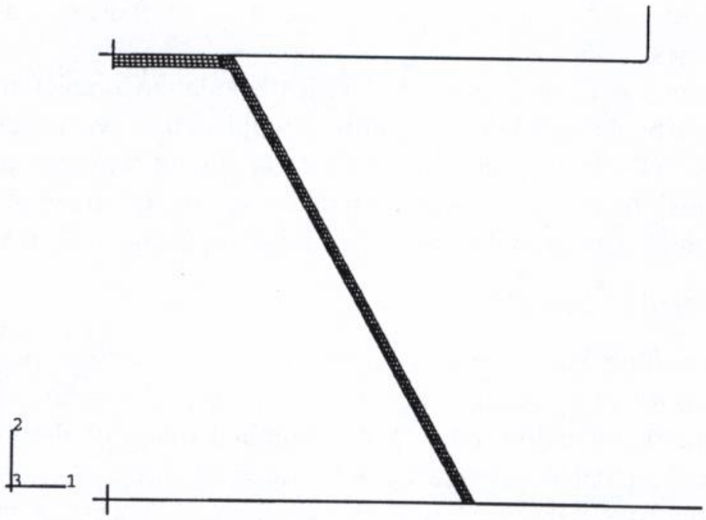

Fig. 1. FE model for outward inversion of frusta.

model. Material properties of the model were taken as rigid perfectly plastic with yield strength $Y = 125$ MPa, mass density, $\rho = 2710\ \text{Kg/m}^3$, Poisson's ratio, $\nu = 0.33$, and Modulus of Elasticity, $E = 70.0$ GPa. All nodes at the centerline of symmetry were selected to move only in the vertical direction.

Both upper and lower surfaces were set in contact with rigid-body surfaces. These rigid surfaces were modeled using two nodal axisymmetric rigid elements, RAX2. A coefficient of friction of $\mu = 0.15$ was incorporated between the contact surfaces. A reference node was introduced at the top end surface of the model. This node was set to move at a velocity of 0.17 mm/s representing the quasi-static case.

The upper small capped-end of the frustum was in contact with a rigid body moving at a constant velocity. The lower end was restrained from moving in the vertical direction as shown in Fig. 1. The axisymmetric elements were chosen to model the axisymmetric collapse of the frusta, and most of the experimentally observed deformation modes were of this type especially at large semi-apical angles and/or large thicknesses.

4. Results and discussions

A large number of frusta, featuring different thicknesses and semi-apex angles were subjected to various loading conditions. Specimens were mainly made from blanks of commercial aluminum; and a few were made of sheet steel and plastic. Frusta, for the experimental program, were produced manually by spinning aluminum sheet of 1.0, 1.5, 2.0, 2.5, and 3.0 mm nominal thickness. Different mandrels, featuring angles (α) of 30°, 40°, 45°, 50°, 55°, 60°, 65°, 70°, and 75° were manufactured for the spinning process. The study involved the use of more than 50 different sizes of frusta made of sheet aluminum, sheet steel and nylon in crushing tests. Tests were conducted by the use of a 10 ton instron universal testing machine (UTM).

Table 1 gives the details of the crushing tests. The table lists experiment number, specimen number, semi-apical angle (ϕ) in degrees, large diameter of the frusta (D) in mm, small diameter

Table 1
Details of the experimental work

No	Sp. No.	ϕ (deg)	D (mm)	H (mm)	d (mm)	D_m (mm)	t (mm)	D_m/t	Mass (g)	P_{av} (N)	E (J)	e (J/g)	Mode	Remark
1	30101	60	73.7	16.0	24.3	49.0	1.0	48.0	13.0	2018	28.26	2.175	I	3 axisymmetric lobes
2	30151	60	71.6	15.0	25.1	48.3	1.4	34.4	16.5	2805	39.28	2.386	I	3 axisymmetric lobes
3	30201	60	73.4	16.0	26.1	49.6	2.0	24.7	24.4	4401	61.61	2.528	I	2 axisymmetric lobes
4	30251	60	72.3	16.0	27.3	49.8	2.6	19.5	29.7	4557	62.89	2.120	I	2 axisymmetric lobes
5	30301	60	71.7	16.0	28.5	50.1	3.2	15.8	35.3	4849	58.18	1.648	I	1 axisymmetric lobe
6	35101	55	69.0	17.0	23.1	46.0	1.0	45.4	11.7	2390	35.85	3.073	II	4 axisymmetric lobes
7	35151	55	69.2	17.0	24.4	46.8	1.4	33.1	15.9	3512	55.49	3.499	II	3 axisymmetric lobes
8	35201	55	69.6	17.0	25.3	47.5	2.0	23.7	22.5	5404	86.46	3.84	II	3 axisymmetric lobes
9	35251	55	72.0	18.0	26.2	49.1	2.6	19.2	30.1	5722	91.55	3.037	II	3 axisymmetric lobes
10	35301	55	72.4	21.0	27.5	50.0	3.0	16.6	37.8	9115	182.3	4.823	II	2 axisymmetric lobes
11	40101	50	70.0	21.0	22.9	46.4	1.0	47.9	12.4	2989	55.60	4.484	II	4 axisymmetric lobes
12	40151	50	71.5	21.0	23.4	47.5	1.4	34.9	17.6	3890	72.35	4.114	II	3 axisymmetric lobes
13	40201	50	73.0	21.0	25.1	49.0	2.0	24.5	25.8	6168	120.9	4.688	II	3 axisymmetric lobes
14	40251	50	72.1	21.0	25.6	48.9	2.4	20.4	30.7	7384	140.3	4.572	II	3 axisymmetric lobes
15	40301	50	72.4	21.0	26.3	49.3	2.9	16.9	36.9	8013	152.2	4.125	II	3 axisymmetric lobes
16	45101	45	70.0	23.0	22.5	46.2	1.0	45.8	13.5	3621	79.67	5.916	II	5 axisymmetric lobes
17	45151	45	71.1	26.0	23.4	47.2	1.3	36.2	18.5	4955	112.0	6.048	II	4 axisymmetric lobes
18	45201	45	73.9	27.0	24.6	49.2	1.9	26.1	28.3	8201	200.1	7.080	II	4 axisymmetric lobes
19	45251	45	73.8	27.0	25.6	49.7	2.4	21.1	35.0	9732	237.5	6.779	II	3 axisymmetric lobes
20	45301	45	74.8	27.0	27.0	50.9	3.0	17.2	43.6	9918	238.0	5.455	II	3 axisymmetric lobes
21	50101	40	69.5	29.0	23.1	46.3	0.9	49.3	13.9	4309	116.4	8.372	II	5 axisymmetric lobes
22	50151	40	72.0	31.0	23.7	47.8	1.3	38.2	20.1	7092	198.6	9.882	II	4 axisymmetric lobes
23	50201	40	73.7	32.0	24.8	49.2	1.8	27.5	29.8	9688	271.3	9.097	II	4 axisymmetric lobes
24	50251	40	73.8	32.0	26.7	50.2	2.2	22.7	37.0	11000	308.0	8.337	II	4 axisymmetric lobes
25	50301	40	74.0	32.0	26.7	50.4	2.7	18.8	45.3	13510	378.4	8.345	II	3 axisymmetric lobes
26	55101	35	72.5	36.0	22.9	47.7	0.9	52.4	16.5	4135	124.0	7.513	III	6 axisymmetric lobes
27	55151	35	70.9	37.0	23.8	47.4	1.2	38.1	21.9	6644	199.3	9.122	II	5 axisymmetric lobes
28	55201	35	72.5	37.0	25.0	48.8	1.8	27.3	31.9	7580	250.1	7.841	II	4 axisymmetric lobes
29	55251	35	74.0	38.0	25.6	49.8	2.1	23.9	38.6	11379	341.4	8.840	II	4 axisymmetric lobes
30	55301	35	73.6	38.0	26.7	50.2	2.6	19.3	47.4	13860	421.3	8.896	II	3 axisymmetric lobes
31	60101	30	72.2	38.0	23.5	47.8	0.9	50.4	17.8	4723	170.0	9.574	III	one 4-sides diamond lobe, followed by 4 axisymmetric lobes
32	60151	30	72.7	44.0	23.5	48.2	1.1	42.0	24.0	7168	258.1	10.75	III	one 4-sides diamond lobe, followed by 3 axisymmetric lobes
33	60201	30	73.7	45.0	25.2	49.4	1.6	31.1	33.5	10180	338.0	10.09	II	2 axisymmetric lobes
34	60251	30	75.5	47.0	25.8	50.7	2	25.2	45.2	10700	406.4	8.997	IV	3 axisymmetric lobes

Table 1 (*continued*)

No	Sp. No.	ϕ (deg)	D (mm)	H (mm)	d (mm)	D_m (mm)	t (mm)	D_m/t	Mass (g)	P_{av} (N)	E (J)	e (J/g)	Mode	Remark
35	60301	30	76.1	48.0	27.0	51.5	2.4	21.4	54.7	13740	533.2	9.756	IV	3 axisymmetric lobes
36	65101	25	72.0	54.0	22.7	47.4	0.8	58.9	19.2	2995	146.1	7.605	IV	one axisymmetric lobe followed by 4 3-sides diamond lobes and ovalisation
37	65151	25	72.5	54.0	23.2	47.9	1.1	43.0	26.8	4772	223.3	8.326	IV	two axisymmetric lobes followed by 2 4-sides diamond lobes and ovalisation
38	65201	25	73.2	55.0	24.3	48.8	1.4	34.3	34.7	7127	314.6	9.027	IV	3 axisymmetric lobes and ovalisation
39	65251	25	74.8	57.0	25.4	50.1	1.9	26.5	48.4	10410	482.9	9.986	IV	3 axisymmetric lobes
40	65301	25	74.7	55.0	26.6	50.6	2.3	21.7	57.6	17070	785.1	13.64	IV	3 axisymmetric lobes
41	70101	20	72.0	69.0	22.8	47.4	0.7	68.4	20.3	2351	138.7	6.836	V	two axisymmetric lobes followed by 2 4-sides diamond lobes and ovalisation
42	70151	20	72.4	68.0	23.2	47.8	1.0	46.2	30.2	4136	248.2	8.221	V	3 axisymmetric lobes followed by 3 3-sides diamond Lobes
43	70201	20	72.9	69.0	24.3	48.6	1.3	37.8	37.9	5211	302.2	7.984	V	3 axisymmetric lobes followed by 2 3-sides diamond lobes and ovalisation
44	75101	15	71.0	94.0	22.0	46.5	0.7	67.7	26.2	2308	191.6	7.307	V	7 axisymmetric lobes followed by 3 4-sides diamond lobes
45	75151	15	73.7	96.0	23.4	48.6	0.9	52.1	37.5	3707	307.7	8.205	V	4 axisymmetric lobes followed 94.0 by 3 3-sides diamond lobes and ovalisation
46	75201	15	74.2	94.0	24.9	49.6	1.3	37.4	52.7	7339	609.2	11.57	V	5 axisymmetric lobes followed by 1 3-sides diamond lobe
47	M6	30	72.0	43.04	21.5	46.8	0.4	110	8.0	1156	42.76	5.345	V	5 4-sided diamond lobes 2
48	M16	30	72.3	43.73	22.0	47.2	0.8	56.8	16.1	3070	113.6	7.054	V	2 axisymmetric lobes followed by 1 3-sides diamond lobes
49	M18	30	73.1	43.73	22.5	47.8	1.3	37.4	26.1	6482	220.4	8.444	II	1 axisymmetric lobes followed by 2 2-sides diamond lobes
50	M32	30	73.4	44.25	23.0	48.2	1.6	30.5	33.8	10740	365.2	10.81	II	3 axisymmetric lobes
51	M42	45	72.0	25.3	21.5	46.8	0.5	102	6.5	1956	38.14	5.868	V	3 4-sides diamond lobe, followed by 1 axisymmetric lobes
52	M55	45	72.8	25.0	22.0	47.4	0.9	50.4	13.6	3980	83.58	6.146	II	one 4-sides diamond lobe, followed by 3 axisymmetric lobes
53	M57	45	73.0	25.10	22.0	47.5	0.9	51.5	13.4	2225	40.04	2.988	II	one 4-sides diamond lobe, followed by 3 axisymmetric lobes
54	M64	45	73.2	25.25	22.5	47.9	1.3	36.9	19.0	6523	117.4	6.180	I	3 axisymmetric lobes
55	M76	45	75.2	25.45	23.0	49.1	1.8	26.7	27.8	11250	258.6	9.303	I	3 axisymmetric lobes
56	M92	60	69.6	14.03	21.5	45.6	0.4	109	4.9	984.6	9.846	2.009	II	2 axisymmetric lobes
57	M102	60	71.2	14.15	22.0	46.6	0.8	54.8	10.0	2253	29.29	2.929	I	3 axisymmetric lobes
58	M112	60	71.6	14.16	22.5	47.1	1.2	38.1	14.5	2686	29.54	1.992	I	3 in series, 3 axisymmetric lobes

Table 1 (*continued*)

59	M113	60	72.1	14.20	22.5	47.3	1.2	38.0	14.9	3453	44.89	3.003	I	2 in series, 3 axisymmetric lobes
60	M115	60	70.5	14.26	22.5	46.5	1.3	35.1	15.1	2686	29.54	1.992	I	3 in series, 3 axisymmetric lobes
61	M116	60	72.2	14.20	22.5	47.4	1.2	39.5	14.3	3155	41.01	2.868	I	3 axisymmetric lobes
62	M119	60	72.5	14.15	22.5	47.5	1.2	38.3	15.0	3453	44.89	3.003	I	2 in series, 3 axisymmetric lobes
63	M120	60	71.8	14.18	22.5	47.2	1.3	37.6	14.9	2686	29.54	1.992	I	3 in series, 3 axisymmetric lobes
64	M121	60	72.2	13.94	23.0	47.6	1.8	26.7	20.9	4929	64.07	3.066	I	2 axisymmetric lobes
65	P30	60	73	70.0	26	49.5	2	24.8	15.4	2913	40.78	2.648	I	Completely inverted upward
66	P45	45	74	27.0	25	49.5	2	24.8	18.8	7976	201.0	10.69	I	Completely inverted upward
67	P60	30	73	16.0	24	48.5	2	24.3	26.4	15080	625.7	23.70	I	Small ovalisation, 1 lobe
68	St30	60	73	70.0	26	49.5	1	49.5	36.8	10740	193.4	5.255	I	2 axisymmetric lobes
69	St45	45	74	27.0	25	49.5	1	49.5	39.2	16180	412.5	10.50	I	3 axisymmetric lobes
70	St60	30	73	16.0	24	48.5	1	48.5	59.8	16650	699.2	11.69	II	2 axisymmetric lobes followed by 1 4-sides diamond lobes

Table 2
Mechanisms of deformation

Mode					
I	Lower end flattening 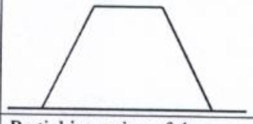	Upward inversion of the lower end 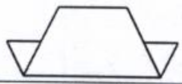	Lower inverted end reaches the upper plate 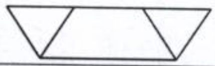	Second inversion of the lower end downward 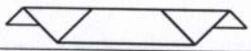	
II	Partial inversion of the upper end 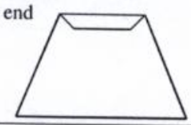	Lower end flattening 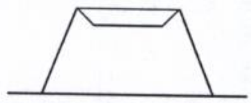	Upward inversion of the lower end 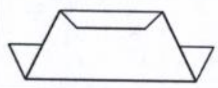	Lower inverted end reaches the upper plate 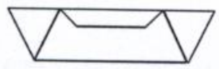	Downward inversion of the lower end 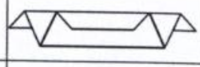
III	Full inversion of the upper end 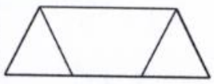	Lower end flattening and upward inversion of the low er end 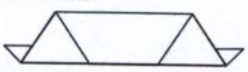	Lower inverted end reaches the upper plate 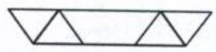	Lower inverted end reaches the lower plate after the second inversion 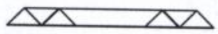	
IV	Formation of the first extensible lobe 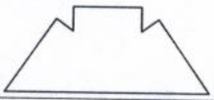	First lobe developed 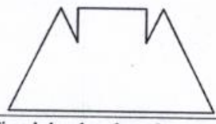	Lower end flattening 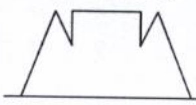	Upward inversion of the lower end 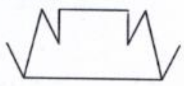	
V	Formation of the first extensible lobe 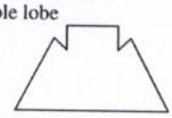	First lobe developed 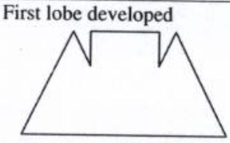	Formation of the first extensible lobe 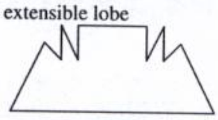	Second lobe developed 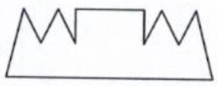	

of the frusta (d) in mm, mean diameter ($D_m = (D + d)/2$) in mm, overall height of the frustum (H) in mm, thickness (t) in mm, D_m/t ratio, mass (m) in grams, experimental average crushing force (P_{av}) in Newton (N), absorbed energy (E) in Joule (J), specific energy (e) in J/g, the deformation mode and remarks if any. The average force is calculated over the whole range of the displacement and the elastic contribution is ignored as a common practice in metallic energy absorbers [8]. In these tests load is applied at the constant crushing speed of 10 mm/min and the specimen is crushed axially until the deformation mode is changed into direct compression of a circular disk.

It was noticed that deformation modes could be classified into:

(a) *Mode I*: Flattening the lower end of the frusta and then curling up or upward inversion of the lower end. The inverted lower end will continue moving up untill it touches the upper plate and re-inverted downward. The frustum continues in this pattern of movement until it becomes a flat disk. Table 2 shows schematic diagrams for the stages of this deformation mode. This mode is limited to aluminum frusta with large semi-apical angle $\phi = 60^\circ$ and a few of 45° angles. All polymer frusta crushed in this fascinating mode as well as steel with large semi-apical angles.

(b) *Mode II*: Partial inward inversion of the upper capped end followed by flattening of the lower end, and then curling up or upward inversion of the lower end. This mode is similar to the first mode; except that it starts with partial inward inversion of the upper end, see Table 2. This mode is observed over a wide range of angles from 55° to 30° for aluminum frusta and 30° for steel frusta.

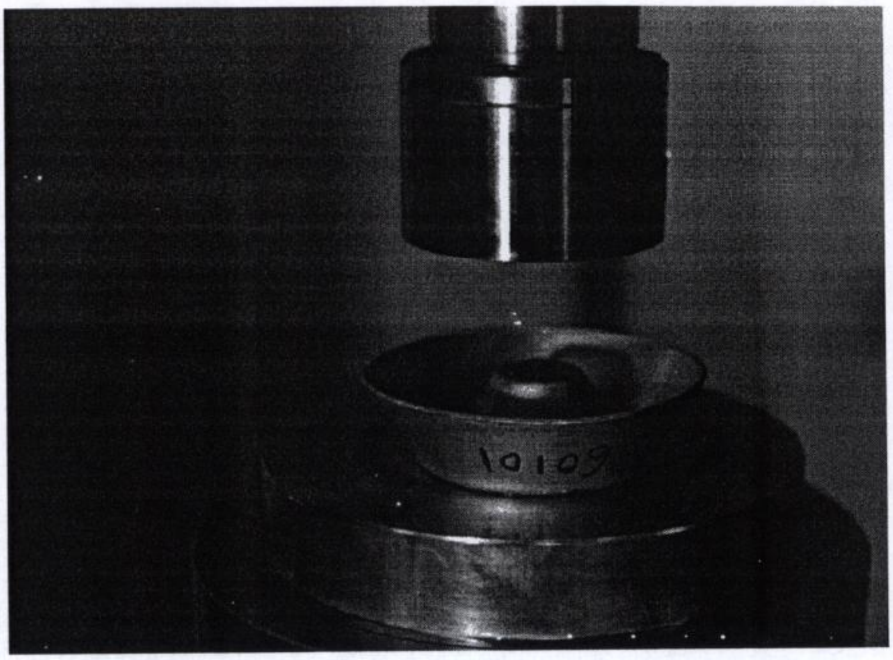

Fig. 2. Photograph showing Specimen 60101 after 22 mm of axial crushing (mode III).

(c) *Mode III*: Full inversion of the upper-capped end until the small end touches the lower plate. Then the deformation mode changes into flattening of the lower end and then curling up or upward inversion of the lower end, as shown in Table 2. This mode is identical to Mode II except that the inward inversion is complete. This mode is limited to a few cases, mainly specimens 55101, 60101 and 60151. Fig. 2 shows a photograph of specimen 60101 after a 22 mm displacement where the upper-capped end is being inverted and it touches the lower plate.

(d) *Mode IV*: Limited extensible collapse mode followed by flattening of the lower end and then curling up or upward inversion of the lower end. This mode is again similar to Modes II and III except that it starts with one or two extensible collapse lobes. This mode is limited to aluminum frusta with different thicknesses at semi-apical angle 25° and thick frusta with a 30° semi-apical angle. Schematic drawings for the stages of this mode are shown in Table 2.

(e) *Mode V*: Full extensible collapse mode. This mode is the only mode investigated in detail in the open literature, see for example, Refs. [2,7]. This mode dominates the deformation pattern at small semi-apical angles 20° and 15° and also reported at thin frusta (thickness less than 1 mm) with semi-apical angles 30° (two cases) and 45° (one case).

The FE details of the crushing process can be seen in Fig. 3 that gives the crushing Mode III of Specimen 60101 in 9 stages. These stages were captured and plotted in Fig. 3 at the following axial intervals: 2.4, 3.6, 6.3, 20, 22, 24, 26, 28 and 31 mm, respectively. The first stage shows the initiation of the inward inversion that continues until the inverted end touches the lower plate as shown in the sixth stage at $x = 24$ mm. Flattening of the lower end is illustrated in the seventh stage, while outward inversion of the lower end is shown in the eighth stage.

Fig. 4 gives the experimental and the finite element load–displacement curves for Specimen 60101. The experimental values are plotted in solid line and it starts from the origin, whereas the FE results

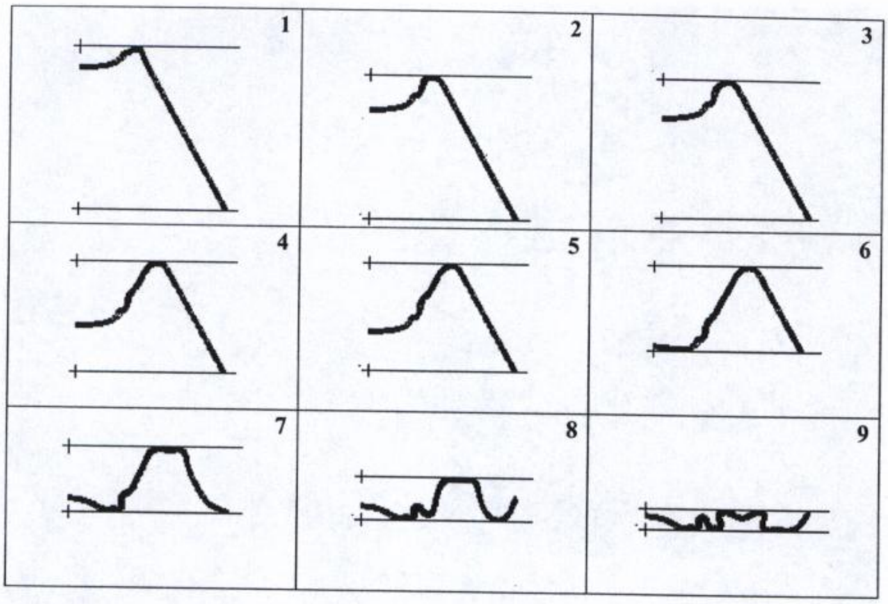

Fig. 3. ABAQUS deformed plots for crushing of aluminum frustum (Specimen 60101, mode III).

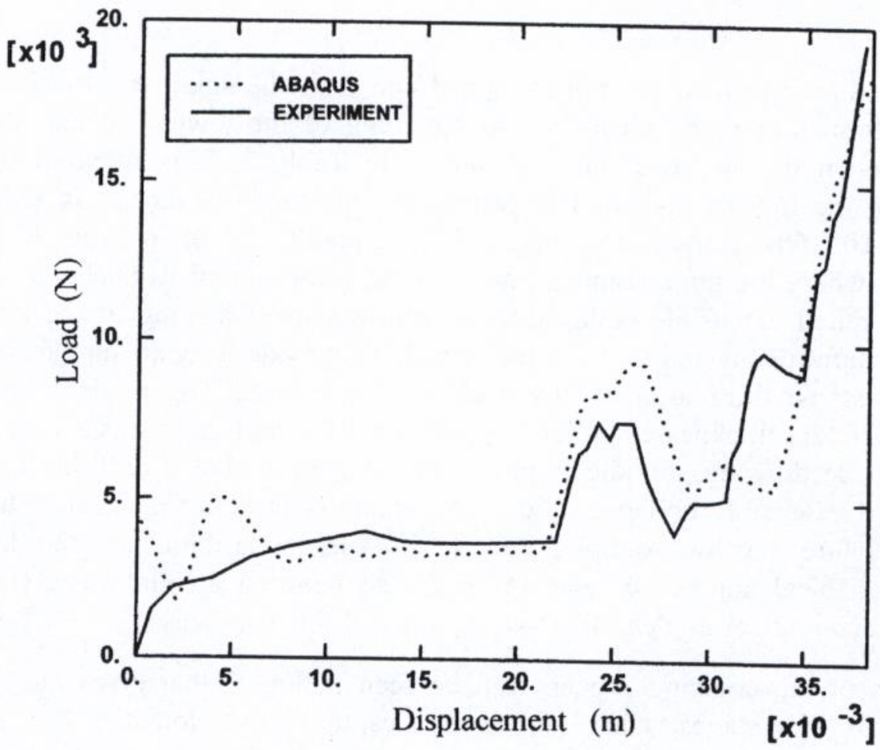

Fig. 4. Experimental and FE load–displacement curves for Specimen 60101.

are plotted in dotted curve and it starts from a non-zero value due to the assumed perfectly plastic material in the FE model. The assumed yield strength in the FE is 125 MPa. Fair agreement between the two curves is shown.

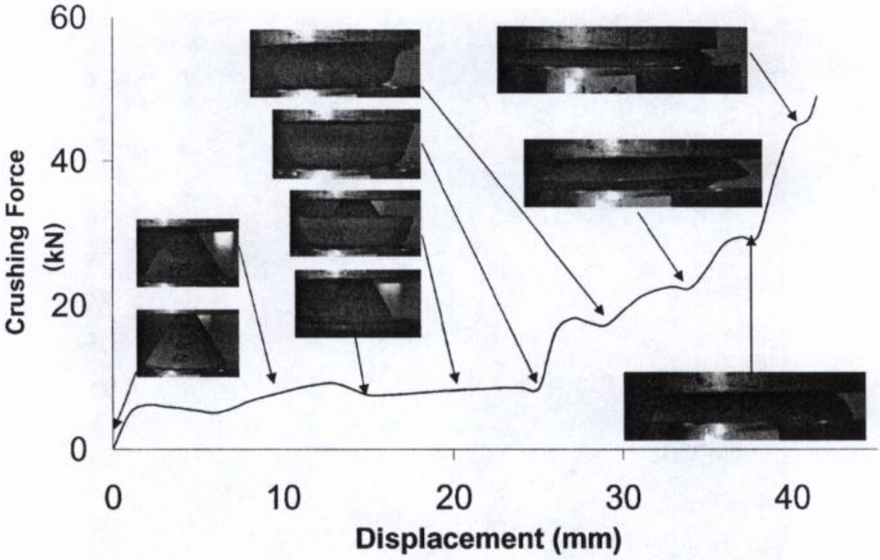

Fig. 5. Load–displacement curve for specimen P60.

Fig. 5 shows the experimental load displacement curve for Specimen P60 with a semi-apical angle of $\phi = 60^\circ$. The specimen was machined from commercial nylon solid bar with an outer diameter of 80 mm. This specimen, when deformed axially, is an excellent example of the first mode, Mode I. The figure contains photographs of the specimen at the following intervals:

(a) At start, at 0 mm.
(b) During flattening of the lower end, at 10 mm.
(c) During outward inversion of the lower end, at 15 and 20 mm.
(d) When the lower inverted end touches the upper plate, at 25 mm.
(e) During re-inversion of the lower end at the upper plate, at 30 and 35 mm.
(f) When the lowered end touches the lower plate at the end of the second stage of inversion, at 38 mm.
(g) At the end, when the crushing mode changes into the compression of a solid circular disk, at 40 mm.

The first 46 aluminum specimens listed in Table 1 are shown in Fig. 6 before and after testing. The bottom photo shows the specimens before the test whereas the top one shows the specimens after the test. The semi-apical angle increases in the photo from left to right, and the thickness increases as you move down. As mentioned in Table 1, one can see that the number of lobes increases with the decrease in wall thickness and semi-apical angle of the frusta.

Fig. 7 shows the plot of the specific energy (energy density) in J/g vs. the semi-apical angle (ϕ) and wall thickness (t). The figure illustrates the effect of angle and thickness changes on the absorbed energy. Generally speaking, one can see that as the semi-apical angle decreases the specific energy increases. The expected value for cylinder ($\phi = 0^\circ$) would represent the upper limit line of this surface. The change in specific energy vs. thickness change is not uniform and does not seem to have a general trend. Although not emphasized here, it is plausible that specific energy may also vary with the overall height of the frustum.

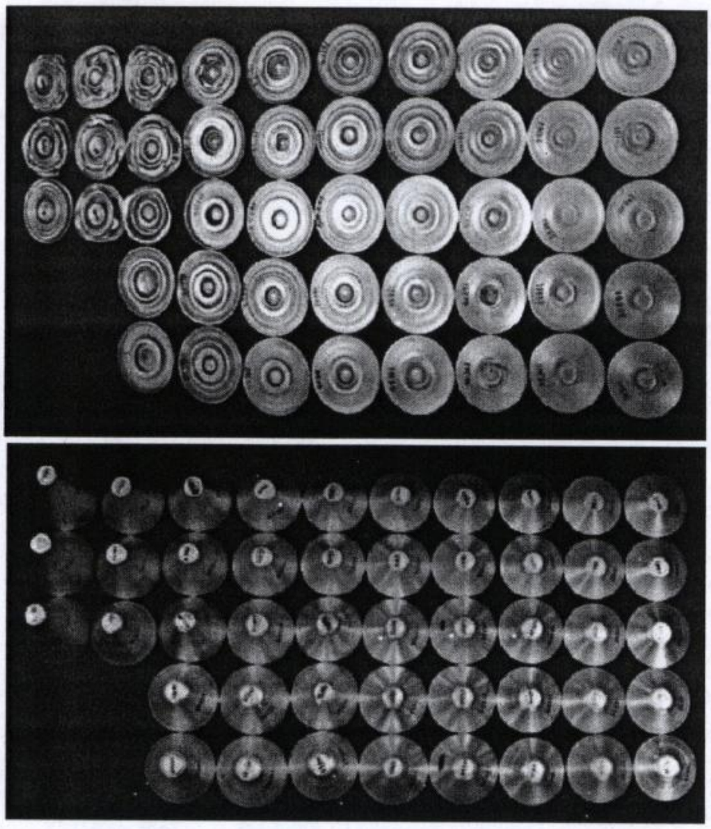

Fig. 6. Aluminum frusta before and after crushing.

4.1. Effect of angle change

Fig. 8 shows the load–displacement curves for specimens with approximately the same thickness ($t = 1$ mm) but with different semi-apical angles $\phi = 55^\circ$, 50°, 45°, and 40° corresponding to Specimens 35101, 40101, 45101 and 50101, respectively. It can be noticed from Table 1 and Fig. 8 that these specimens deformed in Mode II, however, the length of the partial inversion increases with the decrease in the semi-apical angle. These curves are similar to each other, except that the length of the crushing distance increases with the decrease in ϕ. The energy density increases from 3.073 J/g for $\phi = 55^\circ$ to 8.372 J/g for $\phi = 40^\circ$. In conclusion decreasing the semi-apical angle will result in better specific energy.

4.2. Effect of thickness change

Load–displacement curves for specimens with different thicknesses (t) and constant semi-apical angle ($\phi = 40^\circ$) are plotted in Fig. 9. As expected the crushing force increases with the increase in wall thickness. However, energy density increases from 8.372 J/g at $t = 0.9$ mm to a maximum value of 9.882 J/g at $t = 1.3$ mm and then decreases to 8.345 J/g at $t = 2.7$ mm. There is no general trend in the relation between the thickness and the specific energy. These specimens deformed in Mode II and have similar stages, however, the increase in the thickness may postpone the next stage as in

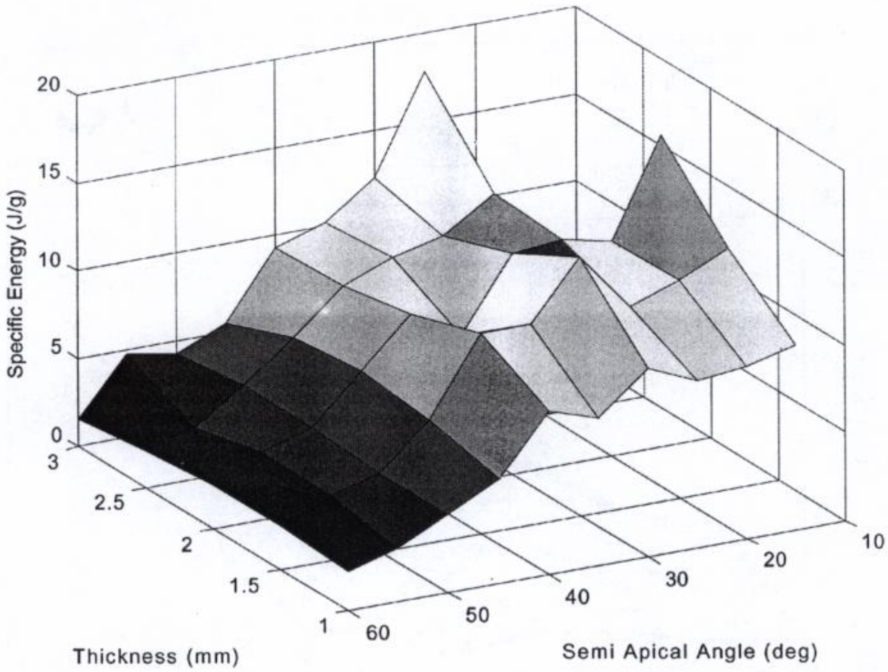

Fig. 7. Specific energy as a function of semi-apical angle and wall thickness of aluminum frusta.

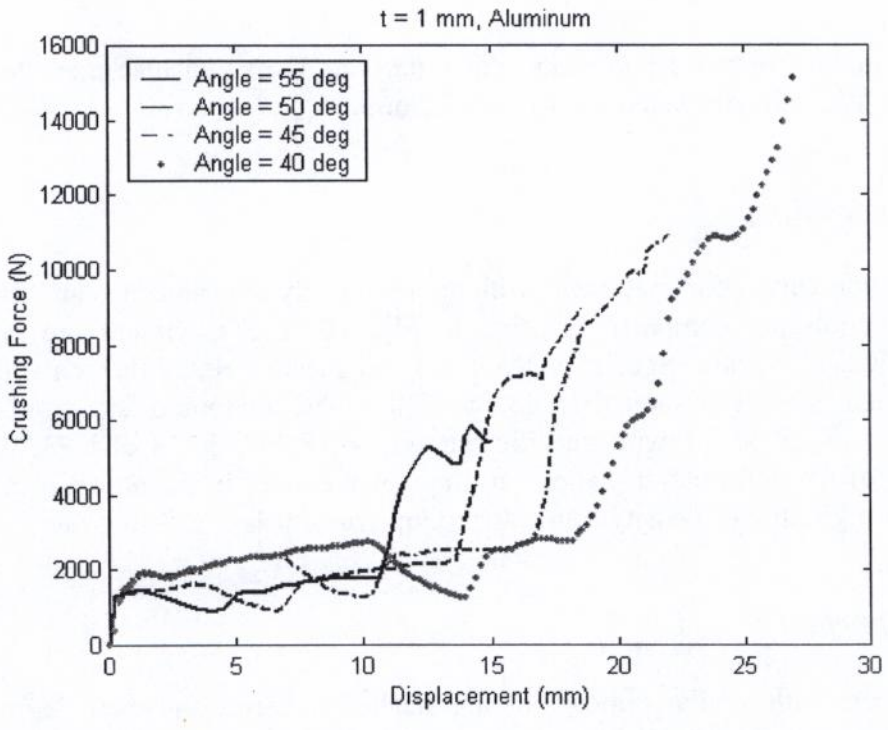

Fig. 8. Effect of semi-apical angle change on the crushing force.

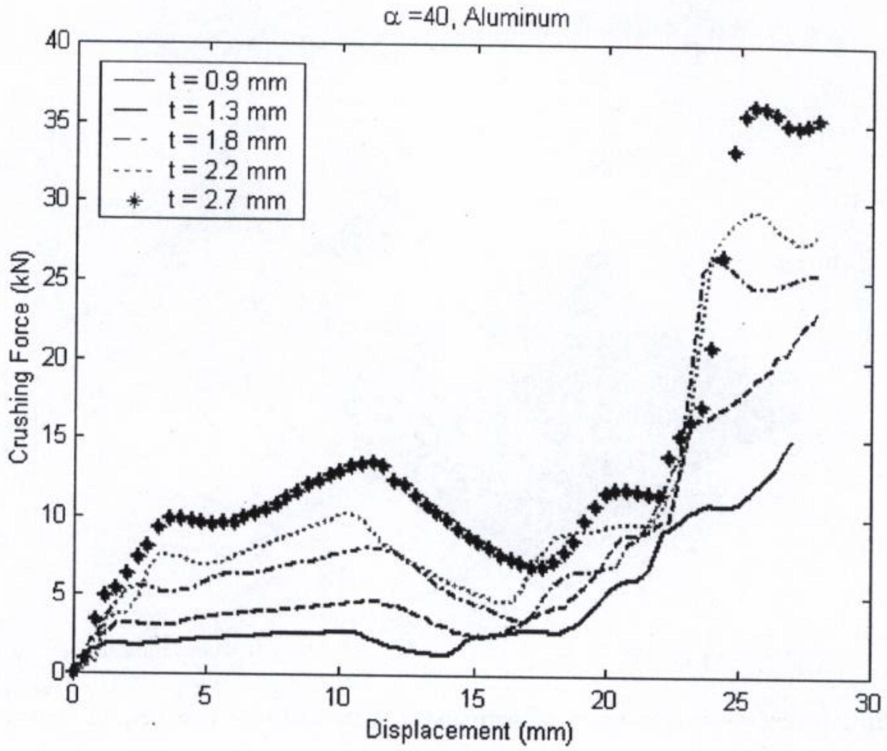

Fig. 9. Effect of thickness change on the crushing force.

the case of the start of outward inversion which starts at 14 mm displacement for $t = 0.9$ mm, but at takes place at 17.5 mm displacement for $t = 2.7$ mm.

4.3. *Effect of material type*

Load–deformation curves for specimens with approximately the same size and same wall thickness but different materials are compared together in Fig. 10. The specimens are made of aluminum (Specimen No. 60251), plastic (Specimen No. P60) and sheet steel and they have the same thickness ($t = 2$ mm) and the same semi-apical angle ($\phi = 30^\circ$). The aluminum, steel and plastic specimens deform in Modes IV, II and I with specific energies of 8.997, 12.14 and 23.70 J/g, respectively. The dependency of the deformation pattern on the material used in the absorber is very clear in this figure. Also, the high energy density value for nylon frustum is a plus for this material.

4.4. *Arrangement effect*

Several absorbers with similar dimensions are stacked in series and their deformation curves are obtained. One, two and three absorbers were tested in series configuration, as seen in Fig. 11 and presented in Table 1. Stacking 2 absorbers in series resulted in better specific energy (3.003 J/g), however, stacking three frusta in series gave a lower value for specific energy (1.992 J/g).

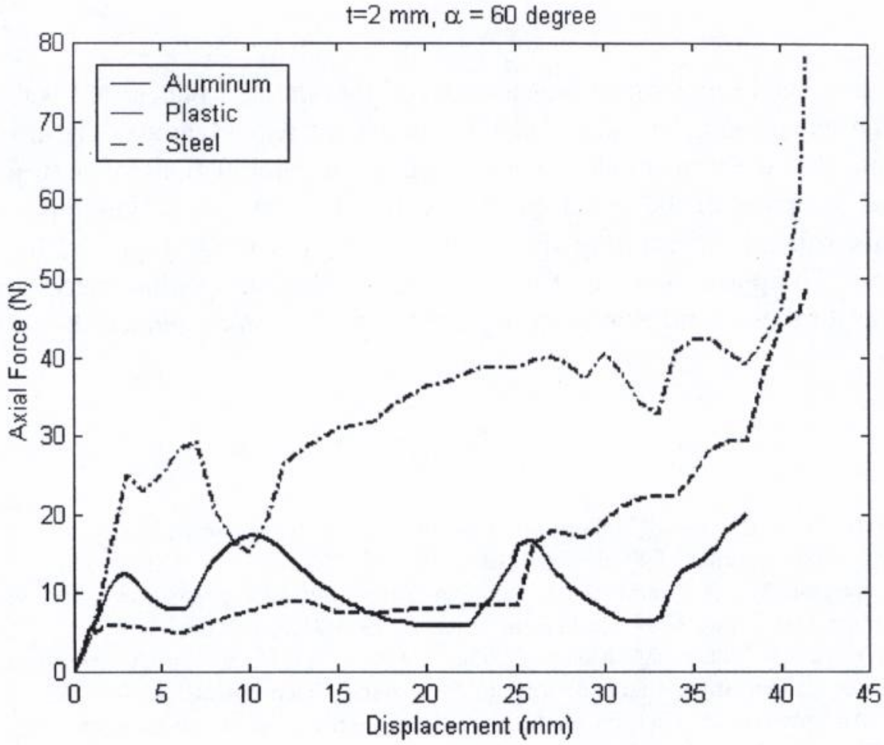

Fig. 10. Effect of material change on the crushing force.

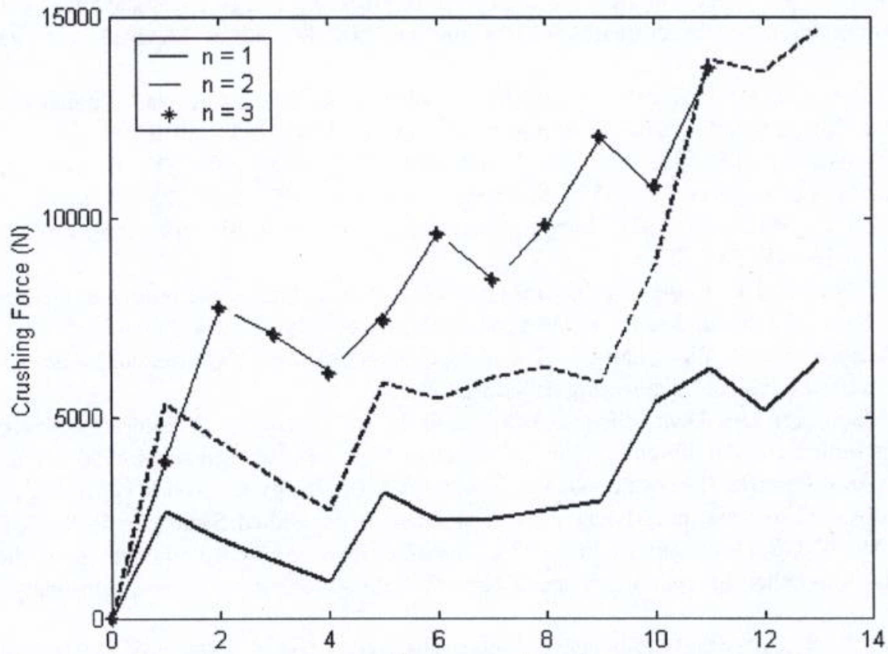

Fig. 11. Effect of series arrangement on the crushing force.

5. Conclusion

This paper studied axial crushing of frusta between two parallel plates. ABAQUS FE results were compared with the experimental results and fair agreement was obtained. The axial collapse modes were classified into five different modes. These modes are combinations of outward inversion of the lower end, inward inversion of the upper end and extensible collapse of the upper end. Material type plays an important role in determining the axial deformation mode followed by semi-apical angle then wall thickness. The plastic (nylon) frusta exhibited a higher specific energy than aluminum and steel frusta. It was further found that stacking frusta in series may reduce the absorbed energy per unit mass.

References

[1] Postlethwaite HE, Mills B. Use of collapsible structural elements as impact isolators with special reference to automotive applications. Journal of Strain Analysis 1970;5:58–73.

[2] Mamalis AG, Johnson W. The quasi-static crumpling of thin-walled circular cylinders and frusta under axial compression. International Journal of Mechanical Sciences 1983;25:713–32.

[3] El-Sobky H, Singace AA, Petsios M. Mode of collapse and energy absorption characteristics of constrained frusta under axial impact loading. International Journal of Mechanical Sciences 2001;43:743–57.

[4] Alexander JM. An approximate analysis of the collapse of thin cylindrical shells under axial loading. Quarternery Journal of Mechanics and Applied Mathematics 1960;13:10–5.

[5] Lu G, Ong LS, Wang B, Ng HW. An experimental study on tearing energy in splitting square metal tubes. International Journal of Mechanical Sciences 1994;36:1087–97.

[6] Johnson W, Reid SR. Metallic energy dissipating systems. Applied Mechanics Reviews 1978;31:277–88.

[7] Mamalis AG, Johnson W, Viegelahn GL. The crumpling of steel thin-walled tubes and frusta under axial compression at elevated strain-rate: some experimental results International Journal of Mechanical Sciences 1984;26(11/12): 537–47.

[8] Mamalis AG, Manolakos DE, Saigal S, Viegelahn G, Johnson W. Extensible plastic collapse of thin-wall frusta as energy absorbers. International Journal of Mechanical Sciences 1986;28(4):219–29.

[9] Mamalis AG, Manolakos DE, Viegelahn GL, Vaxevanidis NM, Johnson W. On the axial collapse of thin-walled PVC conical shells. International Journal of Mechanical Sciences 1986;28(6):323–35.

[10] Johnson W, Soden PD, Al-Hassani STS. Inextensional collapse of thin-walled tubes under axial compression. Journal of Strain Analysis 1977;12:317–30.

[11] Mamalis AG, Manolakos DE, Viegelahn GL, Johnson W. The modeling of the progressive extensible plastic collapse of thin-wall shells. International Journal of Mechanical Sciences 1988;30(3/4):249–61.

[12] Mamalis AG, Manolakos DE, Viegelhan GL. The axial crushing of thin PVC tubes and frusta of square cross-section. International Journal of Impact Engineering 1989;8(3):241–64.

[13] Mamalis AG, Manolakos DE, Demosthenous GA, Ioannidis MB. Analysis of failure mechanisms observed in axial collapse of thin-walled circular fibreglass composite tubes. Thin-Walled Structures 1996;24(4):335–52.

[14] Mamalis AG, Manolakos DE, Demosthenous GA, Ioannidis MB. Energy absorption capability of fibreglass composite square frusta subjected to static and dynamic axial collapse. Thin-Walled Structures 1996;25(4):269–95.

[15] Mamalis AG, Manolakos DE, Demosthenous GA, Ioannidis MB. Analytical modelling of the static and dynamic axial collapse of thin-walled fibreglass composite conical shells. International Journal of Impact Engineering 1997;19: 477–92.

[16] Alghamdi AAA. Design of simple collapsible energy absorber. Master of Science Thesis, College of Engineering, King Abdulaziz University, Jeddah, Saudi Arabia, 1991.

[17] Aljawi AAN, Alghamdi AAA, Abu-Mansour TMN. Details of experimental and finite element analyses for the inversion of capped frusta as impact energy absorbers. International Journal of Impact Engineering, submitted for publication.

[18] Aljawi AAN, Alghamdi AAA. Investigation of axially compressed frusta as impact energy absorbers. In: Gaul L, Brebbia AA, editors. Computational methods in contact mechanics IV. Southampton: WIT Press, 1999. p. 431–43.
[19] Aljawi AAN, Alghamdi AAA. Inversion of frusta as impact energy absorbers. In: Hassan MF, Megahed SM, editors. Current advances in mechanical design and production VII. New York: Pergamon, 2000. p. 511–9.
[20] Alghamdi AAA, Aljawi AAN, Abu-Mansour TMN, Mazi RAA. Axial crushing of frusta between two parallel plates. In: Zhao XL, Grzebieta RH, editors. Structural failure and plasticity, IMPLAST 2000. New York: Pergamon, 2000. p. 545–50.
[21] HKS Inc. ABAQUS/explicit user's manual: theory and examples manual and post manual. Version 5.8, Explicit, 1999.